

Intrinsic Luminescence from Self-Trapped Excitons in $\text{Bi}_4\text{Ge}_3\text{O}_{12}$ and $\text{Bi}_{12}\text{GeO}_{20}$: Decay Kinetics and Multiplication of Electronic Excitations

Minoru ITOH* and Tsuyoshi KATAGIRI[†]

Department of Electrical and Electronic Engineering, Faculty of Engineering,
Shinshu University, Nagano 380-8553

(Received _____)

Abstract

The intrinsic luminescence appearing at 500 nm in $\text{Bi}_4\text{Ge}_3\text{O}_{12}$ (e-BGO) and that at 450 nm in $\text{Bi}_{12}\text{GeO}_{20}$ (s-BGO) have been studied over a wide range of temperature $T = 5\text{--}300$ K by using a Nd:YAG laser and synchrotron radiation as excitation light sources. Luminescence decay curves in e-BGO depend dramatically on the laser power; they are composed of three decay components under high-density excitation, while they show a single exponential decay at low-density excitation. From temperature dependences of the decay time and emission intensity, it is clarified that the triplet state of a self-trapped exciton (STE) responsible for the e-BGO luminescence consists of a pair of closely spaced sublevels with separation energy of 5.7 meV. The decay curves of s-BGO luminescence are essentially nonexponential, irrespective of the excitation power. Time-resolved luminescence measurements of s-BGO suggest the existence of a singlet state lying higher than the triplet STE state. The excitation spectra for the intrinsic luminescence bands have been measured up to 35 eV (35 nm) at 5 K. From the obtained spectra, it is obvious that the multiplication of electronic excitations takes place efficiently in both BGOs. The production processes of multiple excitons are discussed by referring to a recent study on the electronic structures.

PACS Codes: 71.35.Aa, 78.20.-e, 78.47.jd, 78.55.Hx

Keywords: intrinsic luminescence, self-trapped exciton, decay kinetics, multiplication

of electronic excitation, Auger decay, $\text{Bi}_4\text{Ge}_3\text{O}_{12}$, $\text{Bi}_{12}\text{GeO}_{20}$, BGO, synchrotron radiation

*Corresponding author: e-mail: itohlab@shinshu-u.ac.jp

† Present address: GS Yuasa Power Supply Ltd., Minami-ku, Kyoto 601-8520

1. Introduction

Bismuth germanate, $\text{Bi}_4\text{Ge}_3\text{O}_{12}$, is a cubic crystal (space group $I\bar{4}3d$) of the eulytine-type structure, with four formula units per unit cell (Fig. 1(a)).¹⁾ The Bi^{3+} site is coordinated by a distorted octahedron of six oxygen ions. Each Ge ion is surrounded by four equivalent O ions to form $(\text{GeO}_4)^{4-}$ tetrahedra. Bismuth germanium oxide, $\text{Bi}_{12}\text{GeO}_{20}$, is also cubic (space group $I23$), with two formula units per unit cell. It crystallizes in the sillenite-type structure consisting of Bi^{3+} ions coordinated heptahedrally by oxygen ions (Fig. 1(b)).^{2, 3)} Bismuth germanate and bismuth germanium oxide are usually abbreviated as BGO in common. In the present paper we shall call the former e-BGO and the latter s-BGO. The e-BGO is widely used as a scintillation detector, especially in the area of high-resolution PET application,⁴⁾ while the s-BGO has high potential for applications in electro-optic devices.⁵⁾

The luminescence properties of e-BGO have been extensively studied by several groups.^{4, 6-9)} Because of the interest aiming at applying to scintillation detectors, however, these researches are limited at room temperature or $T > 77$ K, except for a few studies down to $T \approx 6$ K.¹⁰⁻¹²⁾ On the other hand, much less attention has been paid to the luminescence properties of s-BGO,^{13, 14)} probably because of the lack of practical interest in them. Very recently, we have measured the reflection, emission-excitation and X-ray photoelectron spectra of e-BGO and s-BGO in the temperature range between 5 and 300 K.¹⁵⁾ The electronic structures of both materials have also been studied by using a relativistic molecular orbital calculation. From the investigations mentioned above, it has been supposed that the intrinsic luminescence bands of e-BGO and s-BGO are ascribed to the radiative recombination of self-trapped excitons (STEs).

It is very interesting to compare the luminescence properties of e-BGO with those of s-BGO, because they have the same elements as constituents but form different crystal structures. The similarity and difference of the obtained results are expected to provide us with useful and detailed information for understanding of their luminescence properties. In the present study, we focus our attention on the luminescence decay kinetics in both BGOs. It is found that the decay curves in e-BGO are composed of three decay components, fast, middle and slow, under high-density excitation of laser pulses, while they simply decay with only the slow component at low-density excitation.

The slow decay time shows an order-of-magnitude increase at low temperatures ($T < 50$ K). This fact is accounted for the presence of a pair of closely spaced triplet sublevels of the STE. The decay curves in s-BGO are also nonexponential, irrespective of the excitation power. The fast decay component in s-BGO is different in nature from that in e-BGO. Time-resolved luminescence measurements on s-BGO suggest that a singlet state lies just above the triplet STE state. Furthermore, excitation spectra for the intrinsic luminescence have been measured up to 35 eV at $T = 5$ K. The multiplication of electronic excitations (MEEs) is found to be efficient in both materials, the processes of which are discussed by reference to the electronic structures calculated by our recent study.¹⁵⁾

2. Experiment

The samples used in the present experiment were freshly cleaved from single-crystalline ingots of e-BGO and s-BGO grown by the Czochralski technique. The e-BGO crystal was completely colorless, while the s-BGO crystal was transparent with a pale yellow color. The origin of this coloration has been discussed in refs. 16 and 17. The samples were mounted on the copper holder in a closed-cycle He optical cryostat, allowing a temperature variation between 5 and 300 K.

Emission and excitation measurements were carried out at the beamline 1B in the UVSOR facility of the Institute for Molecular Science in Okazaki. The incident light from the storage ring was monochromatized with a 1 m VUV monochromator of Seya-Namioka type. Luminescence from the sample surface was dispersed with an Acton SpectraPro-300i monochromator. A liquid-nitrogen cooled ICCD camera was used for measurements of emission spectra, and a photomultiplier for excitation spectra. The emission spectra were not corrected for the spectral response of the detection system, while the excitation spectra were corrected for the intensity distribution of incident light.

Luminescence decay kinetics was detected by a photomultiplier and displayed on a digital storage oscilloscope under the excitation with the fourth harmonics (266 nm; 4.66 eV) of a Q -switched Nd:YAG laser (Continuum Minilite II), having a pulse duration of 7 ns and a repetition rate of 10 Hz. The 266 nm light is located in the exciton-band region of e-BGO and in the interband region of s-BGO.¹⁵⁾ The laser power

density on the sample surface was varied by a suitable combination of metal mesh filters. Time-resolved emission spectra were measured with use of the same detection system as that described in ref. 18.

3. Results

3.1 $Bi_4Ge_3O_{12}$ (e-BGO)

Figure 2 shows the emission spectra of e-BGO excited with VUV light at 150 nm at various temperatures. A peak position locates at 500 nm at $T = 6$ K, with appreciable blue-shift with increasing temperature. The emission intensity at 300 K is less than a tenth that at 6 K. The spectrum at 300 K in Fig. 2 is in good agreement with the earlier result measured at 295 K.⁶⁾

The 500 nm luminescence was also excited by 266 nm photons from a Nd:YAG laser. No changes in spectral shape and peak position were observed when the power density of laser pulses was varied, but its decay kinetics was remarkably power-dependent. The decay kinetics under three different power densities at $T = 8$ K is shown in Fig. 3. When the power density is high (17 MW/cm^2), the decay curve is nonexponential, and is fitted by a sum of three components;

$$I(t) = I_f(0) \exp\left(-\frac{t}{\tau_f}\right) + I_m(0) \exp\left(-\frac{t}{\tau_m}\right) + I_s(0) \exp\left(-\frac{t}{\tau_s}\right), \quad (1)$$

where τ_f , τ_m and τ_s are the fast, middle and slow decay times, respectively, and $I_f(0)$, $I_m(0)$ and $I_s(0)$ are the initial intensities of the respective components at $t = 0$. For the decay curve at 17 MW/cm^2 excitation, we obtain $\tau_f = 1 \text{ } \mu\text{s}$, $\tau_m = 10 \text{ } \mu\text{s}$ and $\tau_s = 110 \text{ } \mu\text{s}$. The fast component becomes weakened with decreasing the power density, and eventually disappears at low-density excitation (0.4 MW/cm^2). As a result, the decay curve is well described by a single exponent, with a decay time $\tau = 120 \text{ } \mu\text{s}$. This value is almost the same as the slow decay time $\tau_s (= 110 \text{ } \mu\text{s})$ estimated at high-density excitation.

Under low-density excitation of 0.4 MW/cm^2 , the decay kinetics of 500 nm luminescence was examined in a wide temperature range from 8 to 300 K. Typical results obtained at relatively low temperatures are depicted in Fig. 4. All the decay curves are single-exponential, with $\tau = 120 \text{ } \mu\text{s}$ (8 K), $82 \text{ } \mu\text{s}$ (14 K), $21 \text{ } \mu\text{s}$ (30 K) and 9

μs (75 K). Such a single-exponential decay was also the case up to $T = 300$ K. It is worth noting that the decay kinetics is purely exponential when the e-BGO crystal is irradiated with a deuterium flash lamp.⁶⁾

Figure 5 shows temperature dependences of the emission intensity (red closed squares; left-hand scale) and decay time (black open circles; right-hand scale) of the 500 nm luminescence. The emission intensity is constant at low temperatures, but decreases at $T > 150$ K due to the onset of nonradiative transition. This dependence is a common feature of the intrinsic luminescence from STEs in many systems.¹⁹⁾ On the other hand, the decay time exhibits a peculiar dependence. The value of τ is constant at low temperatures, but decreases at $T > 10$ K down to a practically constant value at around 100 K. It again starts to abruptly decrease above 150 K, in parallel with the emission intensity. In Fig. 5, red and black lines are the best-fitted curves of eqs. (3) and (4) described later, respectively.

The results of Fig. 5 are very similar to those obtained by Gironnet *et al.*,¹²⁾ who used α -particles as an excitation source. There exists, however, a clear discrepancy between our results and their ones. They observed two decay components, fast and slow, at $T < 150$ K. The fast decay time ($\approx 1 \mu\text{s}$) is nearly temperature-independent, while the slow decay time shows similar temperature dependence to that in Fig. 5. Since α -particles produce conduction electrons (and valence holes) at high density along the central track “core” of ionization,²⁰⁾ the situation under α excitation is likely the same as that under high-density excitation by laser light. A probable reason for the appearance of such a fast decay component at high-density excitation will be discussed later.

The excitation spectrum for 500 nm luminescence at $T = 5$ K is presented in the lower part of Fig. 6. In the upper part of Fig. 6 is also shown the reflection spectrum of e-BGO¹⁵⁾ for the sake of comparison. One may see some dips at 4.8, 14.8, 27.8 and 29.7 eV on the excitation spectrum. They correspond to the exciton reflection peaks, and are, therefore, supposed to originate from reflection losses of the incident light at the sample surface. The 500 nm luminescence is excited with VUV light of the energy coinciding with or exceeding the lowest exciton band. The excitation spectrum of Fig. 6 exhibits an obvious peak at 7.8 eV and a step-like structure at around 11 eV. The emission intensity is further enhanced in the region between 14 and 19 eV, and again in the spectral region

above 21 eV.

3.2 $Bi_{12}GeO_{20}$ (s-BGO)

Figure 7 shows the emission spectra of s-BGO excited with UV light at 266 nm at various temperatures. A peak position locates at 450 nm at $T = 8$ K. The 450 nm luminescence rapidly decreases in intensity with increasing T and disappears above 50 K, leaving behind an emission band peaking at around 500 nm. The 500 nm band is thought not to be intrinsic to s-BGO, and is likely assigned to defect-related luminescence. This defect-related luminescence, having a very long lifetime of ≥ 1 ms, is not quenched up to room temperature.

Decay curves of the 450 nm luminescence under high-density excitation (17 MW/cm²) at $T = 8, 30$ and 45 K are depicted in Fig. 8. They always show a fast decay component of the order of 0.1 μ s. Even if the power density of laser pulses was reduced to 0.4 MW/cm², the decay kinetics was essentially nonexponential, in contrast to e-BGO. The decay curves of Fig. 8 are fitted by eq. (1), as indicated by solid lines. From the fit, the values of τ_f , τ_m and τ_s are estimated to be 0.1 μ s, 8 μ s and 110 μ s at 8 K, 0.1 μ s, 5 μ s and 32 μ s at 30 K, and 0.1 μ s, 2 μ s and 11 μ s at 45 K, respectively. We have to admit an inclusion of large uncertainties (0.04 μ s \sim 0.3 μ s) in the estimate of τ_f .

Figure 9 shows temperature dependences of the emission intensity (red closed squares; left-hand scale) and slow decay time τ_s (black open circles; right-hand scale) of the 450 nm luminescence. Since the slow decay component is the dominant feature of this luminescence, we chose it in Fig. 9. The intensity and decay time are nearly constant at low temperatures, but decreases at $T > 20$ K in parallel to each other. In Fig. 9, black and red lines are the best fits of eqs. (2) and (3) to the experimental data, respectively.

The value of τ_f in s-BGO is significantly smaller ($\sim 1/10$) than that in e-BGO, and is independent of the laser power. Furthermore, in Fig. 8, it is noteworthy that the initial intensity of the fast component in s-BGO is very strong compared to that in e-BGO (Fig. 3). These facts suggest that the fast component in s-BGO is not due to the high-density excitation effect. To clarify the nature of the fast luminescence with $\tau_f \approx 0.1$ μ s, we performed time-resolved luminescence measurements on s-BGO at $T = 8$ K. The

spectrum measured at a delay time $\tau_D = 0$ ns with a gate width of 50 ns is depicted by a red line in Fig. 10, together with that (black line) measured at $\tau_D = 50$ μ s with a gate width of 200 μ s. If the defect-related spectrum is subtracted from the spectrum at 8 K in Fig. 7, one may recognize that the black line spectrum peaking at 450 nm in Fig. 10 is almost identical to the time-integrated emission spectrum in Fig. 7. An interesting finding of Fig. 10 is that the red line spectrum is slightly blue-shifted by 6 nm relative to the black line spectrum.

The excitation spectrum for 450 nm luminescence at $T = 5$ K is presented in the lower part of Fig. 11. In the upper part of Fig. 11 is also shown the reflection spectrum of s-BGO.¹⁵⁾ Overall structures of the excitation spectrum in Fig. 11 closely resemble those in Fig. 6. Some dips due to the reflection losses of incident light are seen at 14.6, 26.1, 27.0 and 29.3 eV on the excitation spectrum. The 450 nm luminescence is excited with photons of the energies above the intrinsic absorption edge. The excitation spectrum of Fig. 11 shows a weak peak at 7.8 eV and a gradual enhancement starting at 10 eV. The emission intensity is sharply increased in the region between 15 and 18 eV, and again in the spectral region above 21 eV.

4. Discussion

4.1 Self-trapped exciton model

For e-BGO, existence of the intrinsic luminescence at 500 nm was confirmed in the 1970s by Weber and Monchamp,⁶⁾ who ascribed it to the radiative recombination of an STE localized on an isolated Bi^{3+} ion. On the basis of a similarity to the luminescence from other materials where trivalent bismuth is present as a dilute activator ion,^{21, 22)} it has been supposed that the energy levels of luminescent Bi^{3+} ions with mercury-like 6s6p excited configuration consist of one singlet state, $^1\text{P}_1$, and three triplet states, $^3\text{P}_2$, $^3\text{P}_1$ and $^3\text{P}_0$, in order of decreasing energy. The ground state is the $^1\text{S}_0$ level. The optical transitions between $^1\text{S}_0$ and $^3\text{P}_2$, $^3\text{P}_1$ or $^3\text{P}_0$ are spin forbidden; however, the level $^3\text{P}_1$ undergoes mixing with $^1\text{P}_1$ by the spin-orbit interaction, making the $^3\text{P}_1 \rightarrow ^1\text{S}_0$ transition observable in luminescence processes. It was, therefore, natural to assign the e-BGO luminescence to the partially allowed $^3\text{P}_1 \rightarrow ^1\text{S}_0$ transition.⁶⁾ This assignment is supported by a recent calculation of the electronic structure of e-BGO,¹⁵⁾ which reveals

that the top of the valence band is formed by O 2p state with substantial contribution from Bi 6s state, and the bottom of the conduction band is almost of Bi 6p character.

The luminescence properties of s-BGO have been studied by Lauer¹³⁾ and Grabmaier and Oberschmid.¹⁴⁾ The former found a broad band at 1.95 eV (636 nm) under the excitation with UV light in the region between 3.2 and 3.6 eV at $T = 80$ K. The latter found two bands at 2.8 eV (443 nm) and 1.8 eV (689 nm) under the excitation with 364 nm (3.41 eV) light from an Ar laser at $T = 1.3$ K. The 636 nm band reported by Lauer is probably of extrinsic origin, because its excitation peak (~ 3.4 eV) is located below the fundamental absorption edge at 3.54 eV (350 nm) of s-BGO. On the other hand, it is not clear whether the 443 nm band reported by Grabmaier and Oberschmid is identical to the 450 nm (or 444 nm) band found by us or not. However, the 443 nm band reported by them may not be intrinsic to s-BGO, because it is excited by photons at 3.41 eV, which again corresponds to the below-edge excitation. Under the below-edge excitation, no luminescence was observed in our s-BGO crystals.

The 450 nm luminescence observed in the present experiment is likely ascribed to the radiative decay of STEs, i.e. the intrinsic luminescence of s-BGO, because it is excited only when the energy of incident photons coincides with or exceeds the lowest exciton band. Because of the long lifetime of 100 μ s, the 450 nm luminescence in s-BGO could be assigned to the partially-allowed radiative transition from a triplet state of the STE.

As noticed in the previous paper,¹⁵⁾ it is a little uncertain whether an exciton in s-BGO is localized well on a Bi³⁺ ion after relaxing into the STE state. This is because the O 2p state substantially contributes to the uppermost valence band, especially in s-BGO. In addition, structural environment around a Bi³⁺ ion is different between s-BGO and e-BGO (see Fig. 1);^{1,2)} (i) the number of oxygen ions surrounding a Bi³⁺ ion is 7 in s-BGO and 6 in e-BGO, and (ii) the interatomic distances of Bi–O in s-BGO are relatively short compared to those in e-BGO. Detailed modeling of the atomic structure of STEs in s-BGO is a future subject to be solved.

In considering the STE model in s-BGO, we have two experimental hints at present. (1) The Stokes-shift of s-BGO luminescence is considerably smaller than that of e-BGO luminescence. The former is about 0.9 eV, and the latter is about 2.3 eV. This fact suggests that the degree of localization of STEs is fairly different between the two

materials, leading to the difference in lattice deformation induced by STEs. (2) In s-BGO, fast-decaying luminescence is observed at 444 nm, in addition to the main slow-decaying luminescence at 450 nm. Taking its decay time of the order of 0.1 μ s into account, such fast luminescence is naturally attributed to the allowed radiative transition from a singlet STE state. No fast luminescence is found in e-BGO, however. There is a possibility that the Stokes shift of the singlet state differs in magnitude from that of the triplet state. This may be the reason why the fast singlet luminescence is not observed in e-BGO. It will be interesting to conduct an optically detected electron paramagnetic resonance (OD-EPR) experiment for s-BGO, in order to investigate the atomic structure of STEs.

4.2 Decay kinetics

Let us now consider the luminescence decay kinetics in e-BGO and s-BGO. The decay curve of e-BGO luminescence deviates increasingly from the exponential law at higher density of excitation. The decay is much faster at the initial stage, and then slows down approaching the single-exponential curve, which coincides with the decay curve at low-density excitation. The situation in s-BGO is more complicated than that in e-BGO, because the fast luminescence peaking at 444 nm overlaps with the slow luminescence at 450 nm, and it lasts even at low-density excitation. Nevertheless, it is obvious that the 450 nm luminescence decays nonexponentially at high-density excitation, as can be seen in Fig. 8, where the decay curves are not fitted by two components but by three.

Nonexponential response under high-density excitation has been found in some insulating materials, such as PbWO_4 ,²³⁾ ZnWO_4 ²⁴⁾ and BaF_2 .²⁵⁾ If the density of STEs is high enough, the dipole-dipole interaction between them leads to a kind of the Auger process, in which one STE decays emitting a virtual photon, whereas after its absorption the other STE is ionized, creating an electron-hole pair. The dipole-dipole interaction leading to fast nonradiative decay of STEs has quite recently been studied theoretically for the case of CdWO_4 in more detail.²⁶⁾

In s-BGO (Fig. 9), the emission intensity and decay time of 450 nm luminescence are both constant at low temperatures and decreased above 20 K. Similar temperature dependences have been found for many luminescence centers in solids.¹⁹⁾ As proposed

by Mott,²⁷⁾ we consider a two-level model that includes an excited and a ground states, on the basis of a configuration-coordinate diagram. In this model, the excited state simply decays through two predominant channels; one is the radiative process with probability of $1/\tau_R$ and the other is the thermally activated nonradiative process to the ground state with probability of $\nu \exp(-\Delta E/k_B T)$, where ν is the frequency factor, ΔE the activation energy and k_B the Boltzmann constant. The decay time $\tau(T)$ is given by

$$\frac{1}{\tau(T)} = \frac{1}{\tau_R} + \nu \exp\left(-\frac{\Delta E}{k_B T}\right). \quad (2)$$

Temperature dependence of the emission intensity is then expressed as

$$I(T) = \frac{\tau(T)}{\tau_R} = [1 + C \exp(-\Delta E / k_B T)]^{-1}, \quad (3)$$

where $C = \tau_R \nu$. Black line in Fig. 9 is the best fit of eq. (2) to the experimental points, with $\Delta E = 12 \pm 2$ meV, $\tau_R = 100 \pm 10$ μ s and $\nu = (1.7 \pm 0.3) \times 10^6$ s⁻¹, and red line is the best-fitted curve of eq. (3), with $\Delta E = 12 \pm 2$ meV and $C = 170 \pm 30$. The agreement between theory and experiment is satisfactory. The obtained values of each parameter are listed in Table I.

Equation (2) cannot explain the decay result of e-BGO luminescence in Fig. 5, which shows dramatic change over an order of magnitude in the temperature range $T = 10$ – 100 K. To explain this observation, we propose a three-level model consisting of two excited states and a ground state, as illustrated in Fig. 12. The two excited states are assignable to the 3P_1 level and the long-lived 3P_0 level. The probabilities of radiative decay from 3P_1 and 3P_0 are given as k_1 and k_0 , respectively ($k_1 \gg k_0$). Both levels are separated by an energy D . The interlevel nonradiative transitions between 3P_1 and 3P_0 take place at rates of k_{10} and k_{01} . Since the rates k_{10} and k_{01} are proportional to $(\langle n \rangle + 1)$ and $\langle n \rangle$, respectively, where $\langle n \rangle = [\exp(D/k_B T) - 1]^{-1}$ is the average phonon density, we will have $k_{01}/k_{10} = \exp(-D/k_B T)$.

There are two distinguishable cases;²¹⁾ (i) $k_{10} \gg k_1$ and $k_{01} \gg k_0$, and (ii) $k_{01} \approx 0$. The case (i) is applicable to the situation where thermal equilibrium between two levels is established and maintained much more rapidly than the decay of either level to the ground state. In such a case, the luminescence decays single-exponentially with only one decay time $\tau(T)$, which is expressed as

$$\frac{1}{\tau(T)} = \frac{k_0 + k_1 \exp(-D/k_B T)}{1 + \exp(-D/k_B T)} + \nu \exp\left(-\frac{\Delta E}{k_B T}\right), \quad (4)$$

adding the thermally activated nonradiative process.^{12, 28)} The case (ii) applies at very low temperatures, in which the luminescence decays bi-exponentially with two decay times of $1/k_0$ and $1/(k_1 + k_{10})$. In fact, coexistence of two decay components has been found for the triplet STE luminescence in KI and RbI,²⁹⁾ and ZnWO₄.²⁴⁾ The decay result of Fig. 5 is fitted well by using eq. (4), as shown by a black curve. The obtained parameters are as follows: $k_0 = (8.2 \pm 0.3) \times 10^3 \text{ s}^{-1}$, $k_1 = (4.1 \pm 0.3) \times 10^5 \text{ s}^{-1}$, $D = 5.7 \pm 0.4 \text{ meV}$, $\nu = (1.1 \pm 0.2) \times 10^8 \text{ s}^{-1}$ and $\Delta E = 100 \pm 5 \text{ meV}$. These values fairly agree with those obtained in ref. 12.

In s-BGO (Fig. 9), the decay time of 450 nm luminescence does not show similar increase to that in Fig. 5, in the low-temperature region down to 8 K. This may suggest that the value of D in s-BGO is considerably smaller than 5.7 meV.

From eq. (4), one can expect to observe a plateau in the temperature dependence of the decay time, if the conditions $D < k_B T$ and $k_B T > \Delta E$ are simultaneously satisfied over a certain temperature range. This is the case, as seen in Fig. 5. The decay time in the plateau region approximately corresponds to τ_R in two-level model. Taking into account the aforementioned proviso $k_1 \gg k_0$, eq. (4) is simplified in the conditions $D < k_B T$ and $k_B T > \Delta E$, and the decay time in the plateau region is determined by the probability of radiative decay from 3P_1 as $\tau_R \approx 2/k_1$. Since $k_1 = (4.1 \pm 0.3) \times 10^5 \text{ s}^{-1}$, we have $\tau_R = 4.9 \pm 0.3 \text{ } \mu\text{s}$ for the e-BGO luminescence.

In three-level model, time-integrated luminescence intensity is proportional to the total population of levels 3P_1 and 3P_0 . Therefore, temperature dependence of the emission intensity in e-BGO is expressed by the same equation as eq. (3) obtained in two-level model. Red line in Fig. 5 is the best-fitted curve of eq. (3), with $\Delta E = 95 \pm 5 \text{ meV}$ and $C = 550 \pm 50$, in good agreement with the experiment.

4.3 Multiplication of electronic excitations

The processes of MEEs have been investigated in alkali halides^{30, 31)} and lead halides.³²⁾ The investigation of MEEs is especially important for e-BGO, because it is widely used as a superior scintillator for high-energy particles. The electronic structures

of e-BGO and s-BGO have been studied in our work.¹⁵⁾ The obtained results are useful for understanding of the processes of MEEs in both materials. Although the overall electronic structure is very similar to each other, there are three main differences between them. (1) The band-gap energy of e-BGO is larger than that of s-BGO; $E_g = 5.26$ eV (e-BGO) and 3.8 eV (s-BGO). (2) The excitonic Bi 6s \rightarrow 6p transition is more intense in e-BGO than in s-BGO. (3) The contribution of Ge⁴⁺ ions in s-BGO is relatively small compared to that in e-BGO. For convenience, a simplified energy-level diagram of e-BGO is illustrated in Fig. 13, where the energy is referred to the top of the valence band. The uppermost valence band is built up by O 2p state, with considerable contribution from Bi 6s state. The full width of the valence band is about 7 eV, which is larger than those in alkali and lead halides.^{31, 32)} The Bi 6s-O 2p hybridized state and the O 2s core state locate at -9 and -18 eV, respectively. The bottom part of the conduction band is mainly formed by Bi 6p state, which splits into $6p_{1/2}$ and $6p_{3/2}$. The Ge 4s and 4p states are situated at 3 and 7 eV above the conduction-band bottom, respectively.

The excitation spectra of e-BGO (Fig. 6) and s-BGO (Fig. 11) rise when excitons are created at $E_{\text{ex}} = 4.81$ and 3.65 eV, respectively. In both materials, a distinct peak is seen at 7.8 eV, where the reflection spectra also exhibit a weak structure. The origin of this peak is not clear, but it may be due to the transition to Bi $6p_{3/2}$ state, locating above Bi $6p_{1/2}$.¹⁵⁾

An inelastic scattering of a sufficiently energetic electron on a valence electron could lead to production of a secondary exciton (or secondary electron-hole pair), with the threshold energy $E_{\text{th}}^1 = E_g + E_{\text{ex}}$, as indicated in Fig. 13. The production of two secondary excitons due to absorption of a photon is also expected to take place at $E_{\text{th}}^2 = 2E_g + E_{\text{ex}}$. The values of E_{th}^1 and E_{th}^2 are estimated to be 10 and 15 eV for e-BGO, and 7 and 11 eV for s-BGO. The excitation spectrum of e-BGO in Fig. 6 indeed shows sharp rises at around 11 and 14 eV. Therefore, these step-like structures are reasonably interpreted as a manifestation of multiple exciton production. On the other hand, the excitation spectrum of s-BGO in Fig. 11 does not show an appreciable rise at 7 eV, and begins to rise gradually at 10 eV. The obscurity of the sharp structures due to multiple exciton production would be explained by assuming that the cross section for electron scattering is low in s-BGO, on the basis that the oscillator strength of exciton transition

is known to be small. A shoulderlike structure is observed at 12 eV in Figs. 6 and 11. This is attributable to the transition to Ge 4p state, which also results in the production of a secondary exciton; see E_{Ge} in Fig. 13.

The emission intensities in both materials are significantly increased in the spectral region between 15 and 18 eV. The optical transitions from Bi 6s-O 2p hybridized state to conduction-band bottom become possible in this region. When a hole is created in the Bi 6s-O 2p hybridized band, it relaxes quickly to the bottom of the valence band. The resulting hot valence hole has a chance that a part of its energy converts into production of a secondary exciton, because the valence-band width is larger than E_{ex} or E_g . This mechanism of MEE, which is indicated as E_{e1} , could explain the intensity enhancement in the 15–18 eV range.

The emission intensities in both materials are again increased in the region above 21 eV. In this case, a hot valence hole resulting from quick relaxation of a core hole created in the O 2s band will participate in the production process of a secondary exciton; see E_{e2} in Fig. 13. The MEEs of Auger-type may also be possible, because the energy separation between the bottom of Bi 6s-O 2p band and the top of O 2s band is comparable to or somewhat larger than E_g . We suppose that a core hole created in the O 2s band relaxes to the Bi 6s-O 2p band by kicking up a valence electron into the conduction band, thus forming a secondary exciton.

Three distinct peaks are observed at around 26, 27 and 29 eV in the reflection spectra of both BGOs. They are attributed to the cationic core exciton transitions Bi 5d \rightarrow 6p (not shown in Fig. 13). The formation of secondary excitons due to the nonradiative decay of these core excitons is supposed to appear superpositionally on the background signals due to other mechanisms of MEEs. Such an enhancement in emission intensity, however, is not seen in the 25–30 eV range. It is probable that the cationic core exciton efficiently Auger-decays with ejecting a photoelectron from the crystal into a vacuum.

5. Summary

In the present study, we have investigated the luminescence decay kinetics in e-BGO and s-BGO by using a Nd:YAG laser. It is found that the decay curves in e-BGO consist of three decay components under high-density excitation, while they simply decay with

only the slow component at low-density excitation. The slow decay time shows an order-of-magnitude increase at low temperatures. This fact is accounted for the presence of a pair of closely spaced sublevels of triplet STE state. The decay curves of s-BGO luminescence are essentially nonexponential, irrespective of the excitation power. The result of time-resolved luminescence measurements in s-BGO suggests the existence of a singlet state lying higher than the triplet STE state. The excitation spectra for e-BGO and s-BGO luminescence have been measured up to 35 eV by using synchrotron radiation. It is confirmed that the processes of MEEs play a significant role in both materials. Various types of MEE mechanisms are proposed to explain the experimental data. Finally, it is pointed out that the STE in e-BGO is localized on a Bi^{3+} ion, while the atomic structure of STE in s-BGO remains still open.

Acknowledgements

The authors would like to acknowledge Dr. Y. Usuki for kindly providing the single-crystalline ingots of e-BGO and s-BGO used in the present study. They are also grateful to Mr. Y. Takizawa, Mr. K. Goto and Mr. K. Kasashima for their assistance in the experiments. A part of this work was supported by the Joint Studies Program of the Institute for Molecular Science.

References

- 1) P. Fischer and F. Waldner: Solid State Commun. **44** (1982) 657.
- 2) S. C. Abrahams, P. B. Jamieson and J. L. Bernstein: J. Chem. Phys. **47** (1967) 4034.
- 3) E. Suzuki, N. Iyi and K. Kitamura: J. Korean Phys. Soc. **32** (1998) S173.
- 4) Z. H. Cho and M. R. Farukhi: J. Nucl. Med. **18** (1977) 840.
- 5) P. V. Lenzo, E. G. Spencer and A. A. Ballman: Phys. Rev. Lett. **19** (1967) 641.
- 6) M. J. Weber and R. R. Monchamp: J. Appl. Phys. **44** (1973) 5495.
- 7) H. V. Piltingsrud: J. Nucl. Med. **20** (1979) 1279.
- 8) V. Y. Ivanov, A. V. Kruzhalov, V. A. Pustovarov and V. L. Petrov: Nucl. Instrum. Methods Phys. Res. A **261** (1987) 150.
- 9) P. Lecoq, M. Schussler and M. Schneegans: Nucl. Instrum. Methods Phys. Res. A **315** (1992) 337.
- 10) F. Rogemond, C. Pedrini, B. Moine and G. Boulon: J. Lumin. **33** (1985) 455.
- 11) Z. H. Cho, M. D. Petroff and R. Bharat: IEEE Trans. Nucl. Sci. **38** (1991) 1786.
- 12) J. Gironnet, V. B. Mikhailik, H. Kraus, P. de Marcillac and N. Coron: Nucl. Instrum. Methods Phys. Res. A **594** (2008) 358.
- 13) R. B. Lauer: Appl. Phys. Lett. **17** (1970) 178.
- 14) B. C. Grabmaier and R. Oberschmid: Phys. Status Solidi A **96** (1986) 199.
- 15) M. Itoh, T. Katagiri, H. Mitani, M. Fujita and Y. Usuki: Phys. Status Solidi B **245** (2008) 2733.
- 16) S. L. Hou, R. B. Lauer and R. E. Aldrich: J. Appl. Phys. **44** (1973) 2652.
- 17) R. Oberschmid: Phys. Status Solidi A **89** (1985) 263.
- 18) M. Itoh and T. Aoki: J. Phys.: Condens. Matter **22** (2010) 045503.
- 19) K. S. Song and R. T. Williams: *Self-Trapped Excitons* (Springer-Verlag, Berlin, 1993).
- 20) S. P. Ahlen: Rev. Mod. Phys. **52** (1980) 121.
- 21) A. E. Hughes and G. P. Pells: Phys. Status Solidi B **71** (1975) 707.
- 22) Y. Porter-Chapman, E. Bourret-Courchesne and S. E. Derenzo: J. Lumin. **128** (2008) 87.
- 23) M. Itoh, M. Horimoto and M. Fujita: J. Phys.: Condens. Matter **15** (2003) 193.
- 24) M. Itoh, T. Katagiri, T. Aoki and M. Fujita: Radiat. Meas. **42** (2007) 545.
- 25) K. Kimura and J. Wada: Phys. Rev. B **48** (1993) 15535.

- 26) M. Kirm, V. Nagirnyi, E. Feldbach, M. de Grazia, B. Carré, H. Merdji, S. Guizard, G. Geoffroy, J. Gaudin, N. Fedorov, P. Martin, A. Vasil'ev and A. Belsky: *Phys. Rev. B* **79** (2009) 233103.
- 27) N. F. Mott: *Proc. Roy. Soc. London A* **167** (1938) 384.
- 28) V. B. Mikhailik, H. Kraus, S. Henry and A. J. B. Tolhurst: *Phys. Rev. B* **75** (2007) 184308.
- 29) J. U. Fischbach, D. Fröhlich and M. N. Kabler: *J. Lumin.* **6** (1973) 29.
- 30) J. H. Beaumont, A. J. Bourdillon and M. N. Kabler: *J. Phys. C: Solid State Phys.* **9** (1976) 2961.
- 31) A. Lushchik, E. Feldbach, R. Kink, Ch. Lushchik, M. Kirm and I. Martinson: *Phys. Rev. B* **53** (1996) 5379.
- 32) M. Kitaura, M. Itoh, H. Nakagawa and M. Fujita: *J. Phys. Soc. Jpn.* **72** (2003) 730.

Figure captions

Fig. 1. (Color online) Crystal structures of (a) $\text{Bi}_4\text{Ge}_3\text{O}_{12}$ (e-BGO) and (b) $\text{Bi}_{12}\text{GeO}_{20}$ (s-BGO) with respect to the [100], [010] and [001] axes. Large blue, middle red and small green circles indicate Bi^{3+} , Ge^{4+} and O^{2-} ions, respectively. The bonds of $(\text{GeO}_4)^{4-}$ tetrahedra are indicated as thin lines. The lattice constants of e-BGO and s-BGO are 10.513 and 10.147 Å, respectively.

Fig. 2. (Color online) Emission spectra of e-BGO excited with 150 nm light at various temperatures. The peak intensity at $T = 6$ K is normalized to unity.

Fig. 3. (Color online) Decay kinetics of the 500 nm luminescence in e-BGO under three different power densities (17, 2.7 and 0.4 MW/cm^2) of laser light at $T = 8$ K. Each decay curve is vertically displaced for the sake of clarity.

Fig. 4. (Color online) Decay kinetics of the 500 nm luminescence in e-BGO at low-density excitation of 0.4 MW/cm^2 at $T = 8, 14, 30$ and 75 K. The initial intensities at $t = 0$ are normalized to unity.

Fig. 5. (Color online) Temperature dependences of the 500 nm luminescence in e-BGO; emission intensity (red closed squares; left-hand scale) and decay time (black open circles; right-hand scale). Red and black lines are the best-fitted curves of eqs. (3) and (4), respectively.

Fig. 6. Excitation spectrum for the 500 nm luminescence in e-BGO at $T = 5$ K is presented in the lower part. The reflection spectrum of e-BGO observed in ref. 15 is also shown in the upper part for comparison. The threshold energies for various types of MEEs are indicated as E_{th}^1 , E_{th}^2 , E_{Ge} , E_{e1} and E_{e2} , respectively.

Fig. 7. (Color online) Emission spectra of s-BGO excited with 266 nm light at various temperatures. The peak intensity at $T = 8$ K is normalized to unity.

Fig. 8. (Color online) Decay kinetics of the 450 nm luminescence in s-BGO under high-density excitation of 17 MW/cm^2 at $T = 8, 30$ and 45 K . Each decay curve is vertically displaced for the sake of clarity. Solid curves are the best fit of eq. (1) to the data.

Fig. 9. (Color online) Temperature dependences of the 450 nm luminescence in s-BGO; emission intensity (red closed squares; left-hand scale) and decay time (black open circles; right-hand scale). Black and red lines are the best-fitted curves of eqs. (2) and (3), respectively.

Fig. 10. (Color online) Time-resolved luminescence spectra of s-BGO at $T = 8 \text{ K}$. The red line spectrum was measured at a delay time $\tau_D = 0 \text{ ns}$ with a gate width of 50 ns , and the black line spectrum at $\tau_D = 50 \mu\text{s}$ with a gate width of $200 \mu\text{s}$. The peak intensities of red and black line spectra are normalized to unity.

Fig. 11. Excitation spectrum for the 450 nm luminescence in s-BGO at $T = 5 \text{ K}$ is presented in the lower part. The reflection spectrum of s-BGO observed in ref. 15 is also shown in the upper part for comparison. The threshold energies for various types of MEEs are indicated as E_{th}^1 , E_{th}^2 , E_{Ge} , E_{e1} and E_{e2} , respectively.

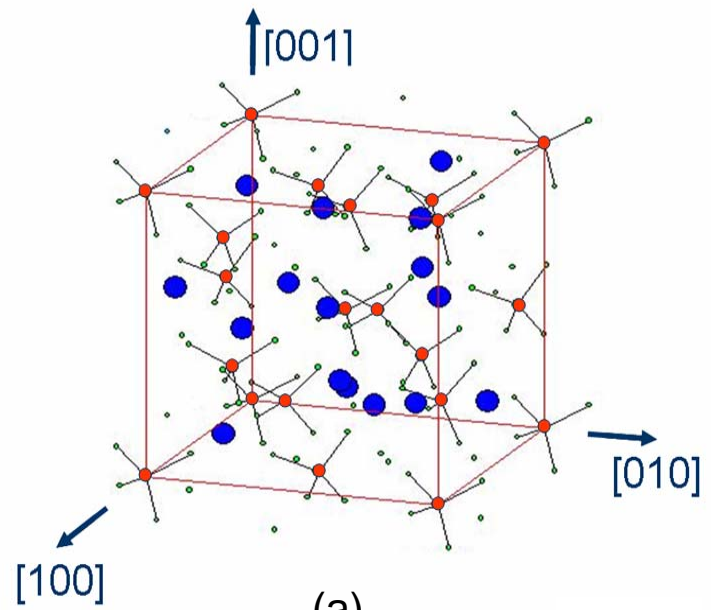
Fig. 12. A three-level model for the e-BGO luminescence. The probabilities of radiative decay from the excited levels $^3\text{P}_1$ and $^3\text{P}_0$ separated by an energy D to the ground state $^1\text{S}_0$ are given as k_1 and k_0 , respectively. Interlevel nonradiative transitions with rates k_{10} and k_{01} are also taken into account. Thermally activated nonradiative process with probability of $\nu \exp(-\Delta E/k_B T)$ is added.

Fig. 13. (Color online) Simplified energy-level diagram of e-BGO. The energy is referred to the top of the valence band. Various types of MEEs are depicted by broken arrows. The details are described in the text.

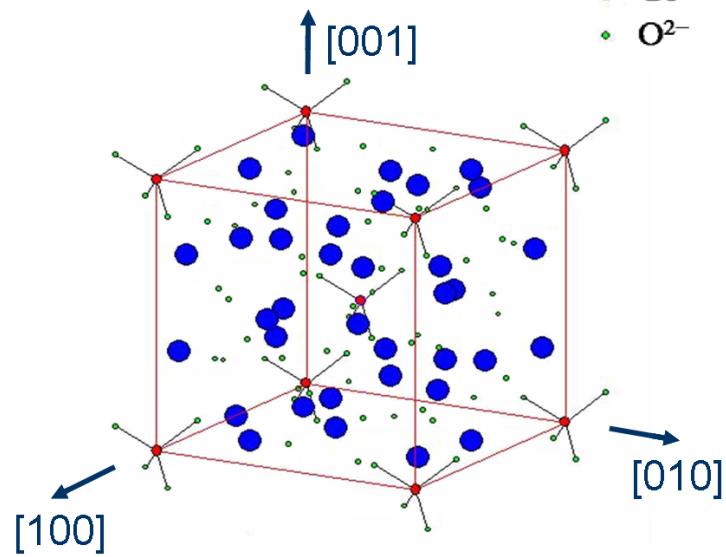
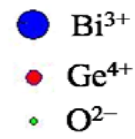
Table I. Experimentally determined parameters of the triplet STE luminescence in e-BGO and s-BGO. τ_R : radiative decay time, k_0 : probability of radiative decay from 3P_0 , k_1 : probability of radiative decay from 3P_1 , D : energy distance between 3P_1 and 3P_0 , ν : frequency factor and ΔE : activation energy. The values of e-BGO obtained in ref. 12 are presented in parentheses.

Material	τ_R (s)	k_0 (s^{-1})	k_1 (s^{-1})	D (meV)	ν (s^{-1})	ΔE (meV)
e-BGO	4.9×10^{-6}	8.2×10^3 (7.5×10^3)	4.1×10^5 (4.5×10^5)	5.7 (6.4)	1.1×10^8 (1.3×10^8)	95 or 100 (105)
s-BGO	100×10^{-6}				1.7×10^6	12

Figure 1



(a)



(b)

Figure 2

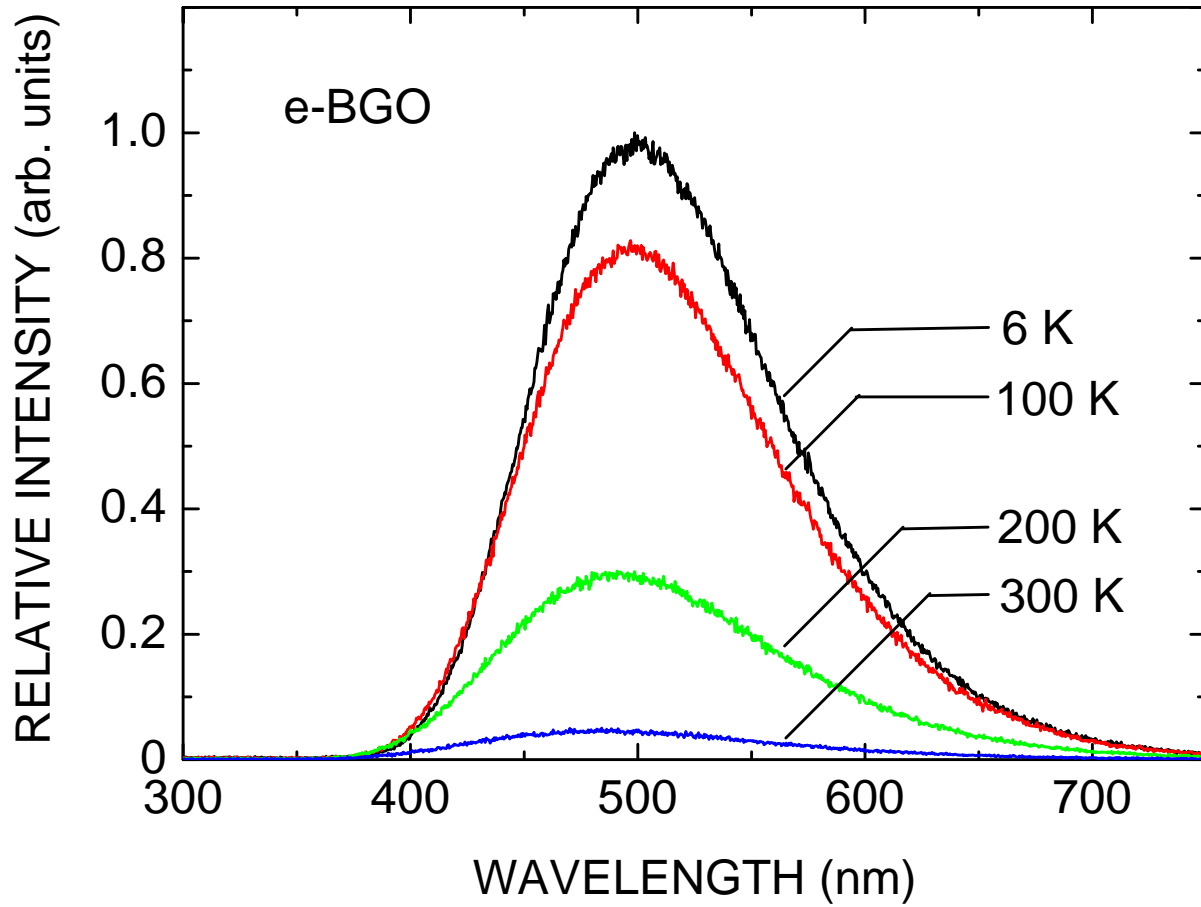


Figure 3

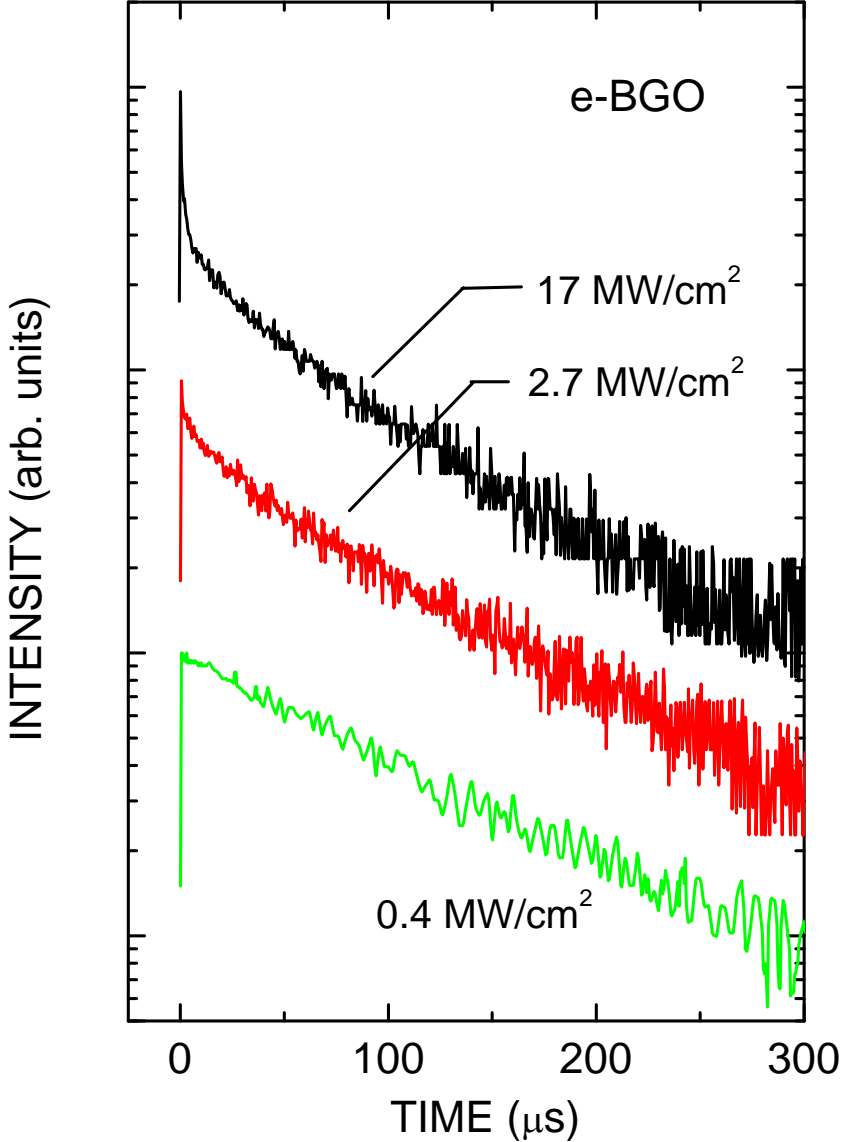


Figure 4

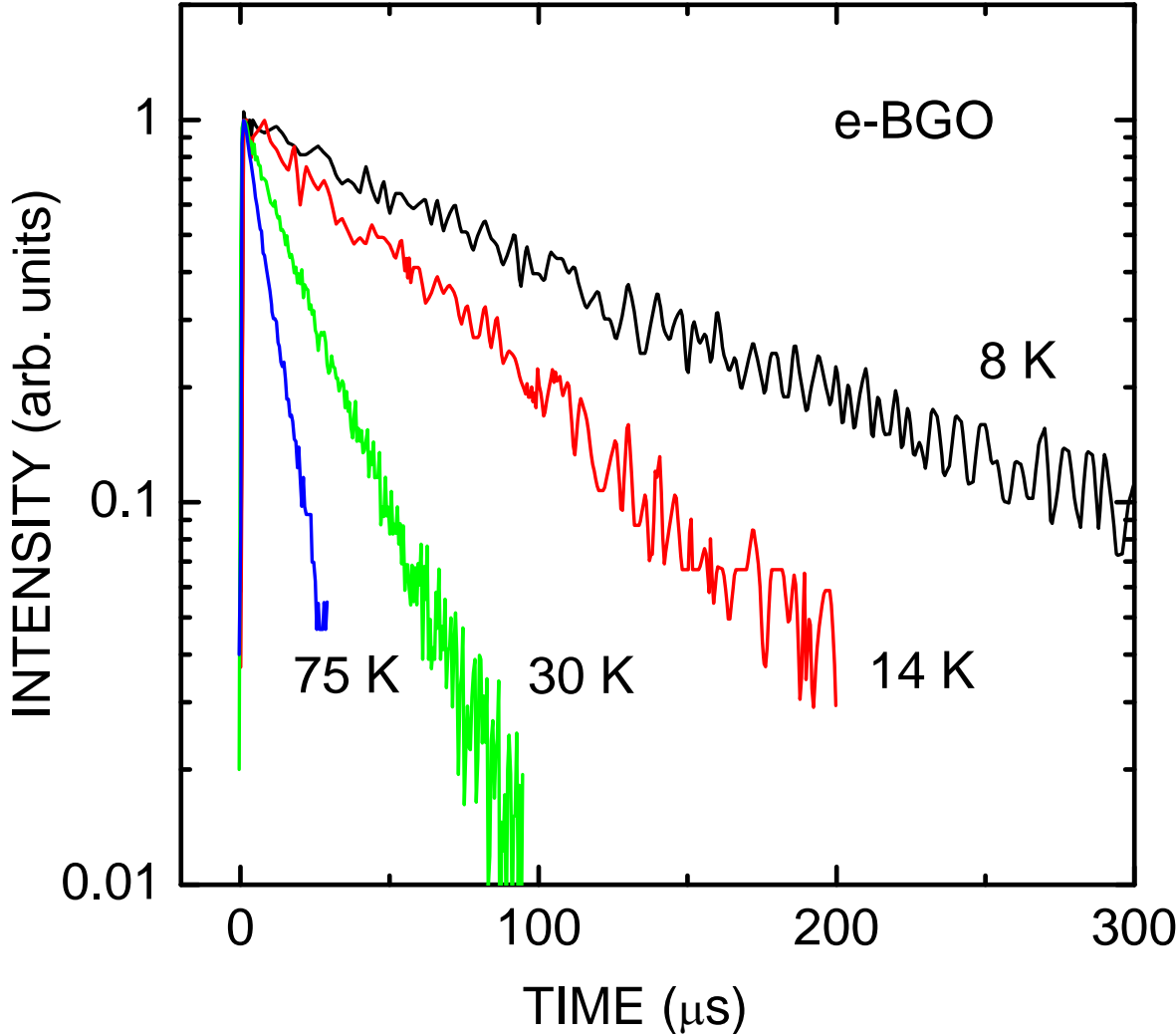


Figure 5

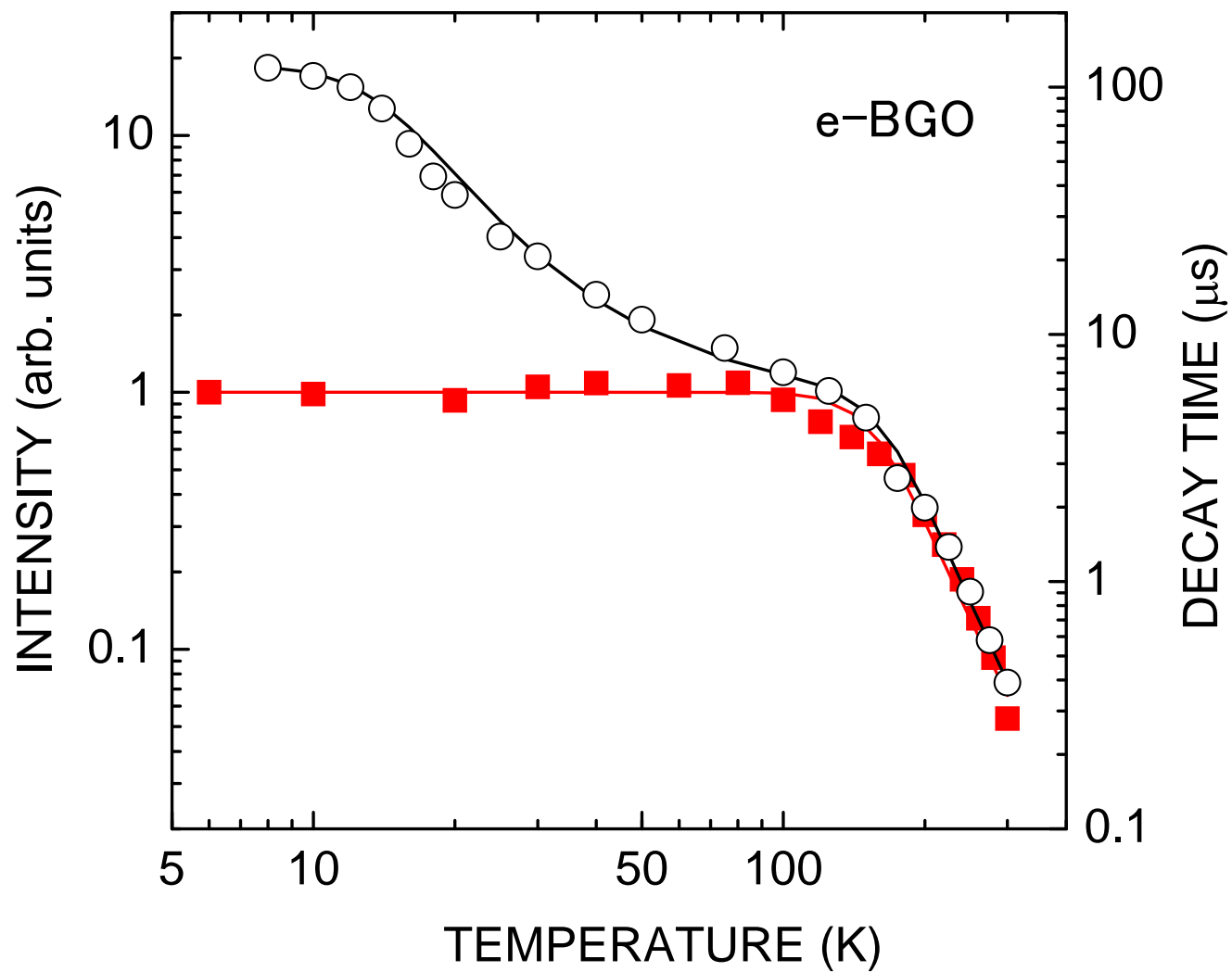


Figure 6

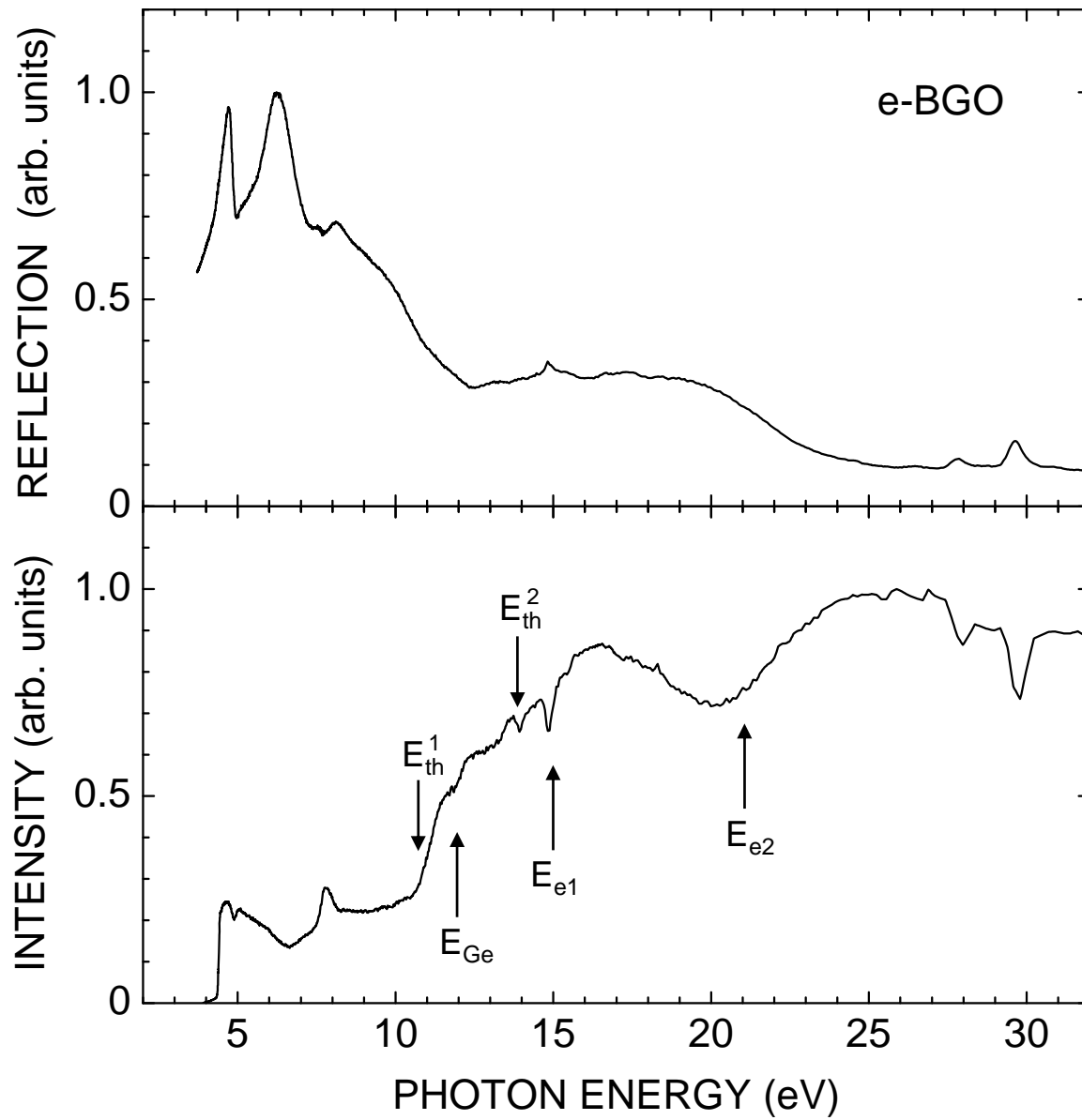


Figure 7

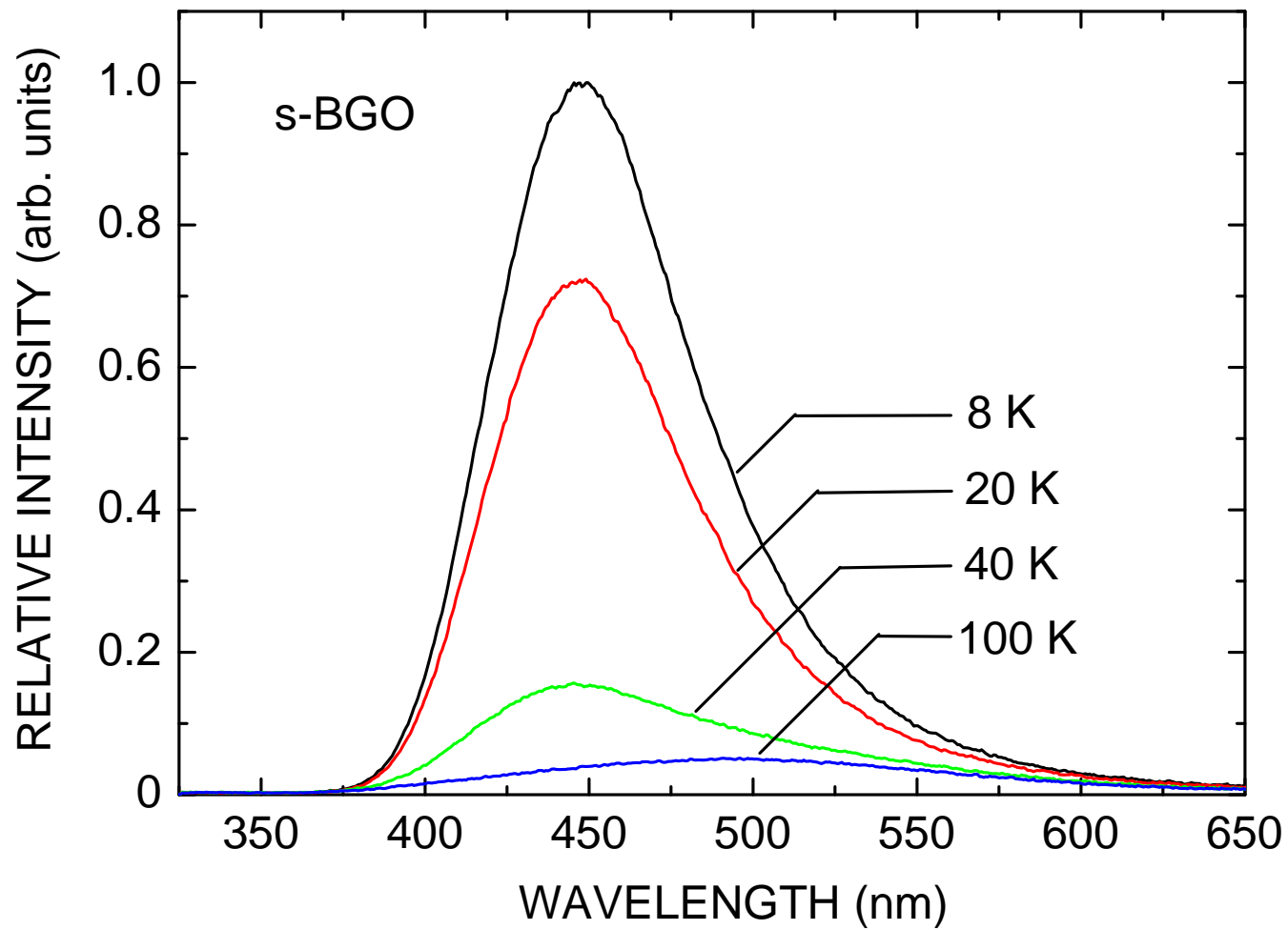


Figure 8

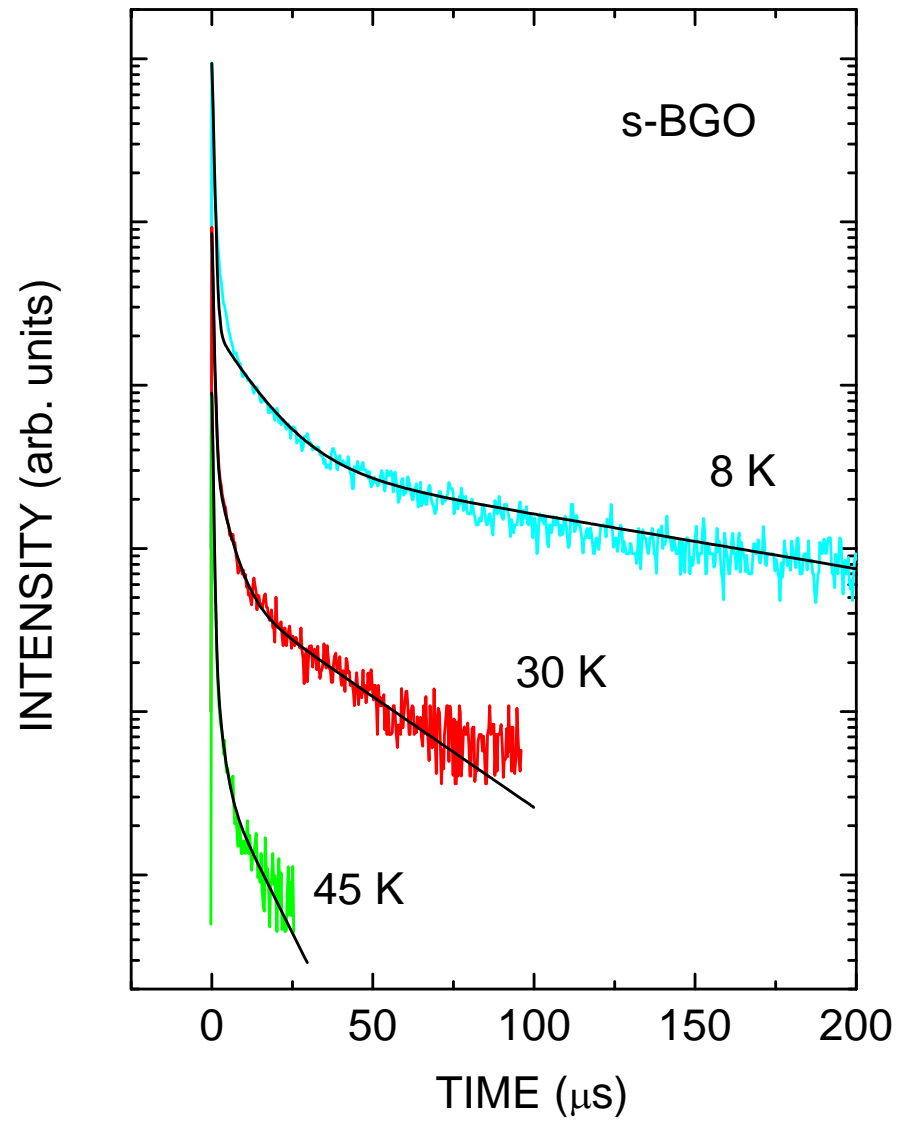


Figure 9

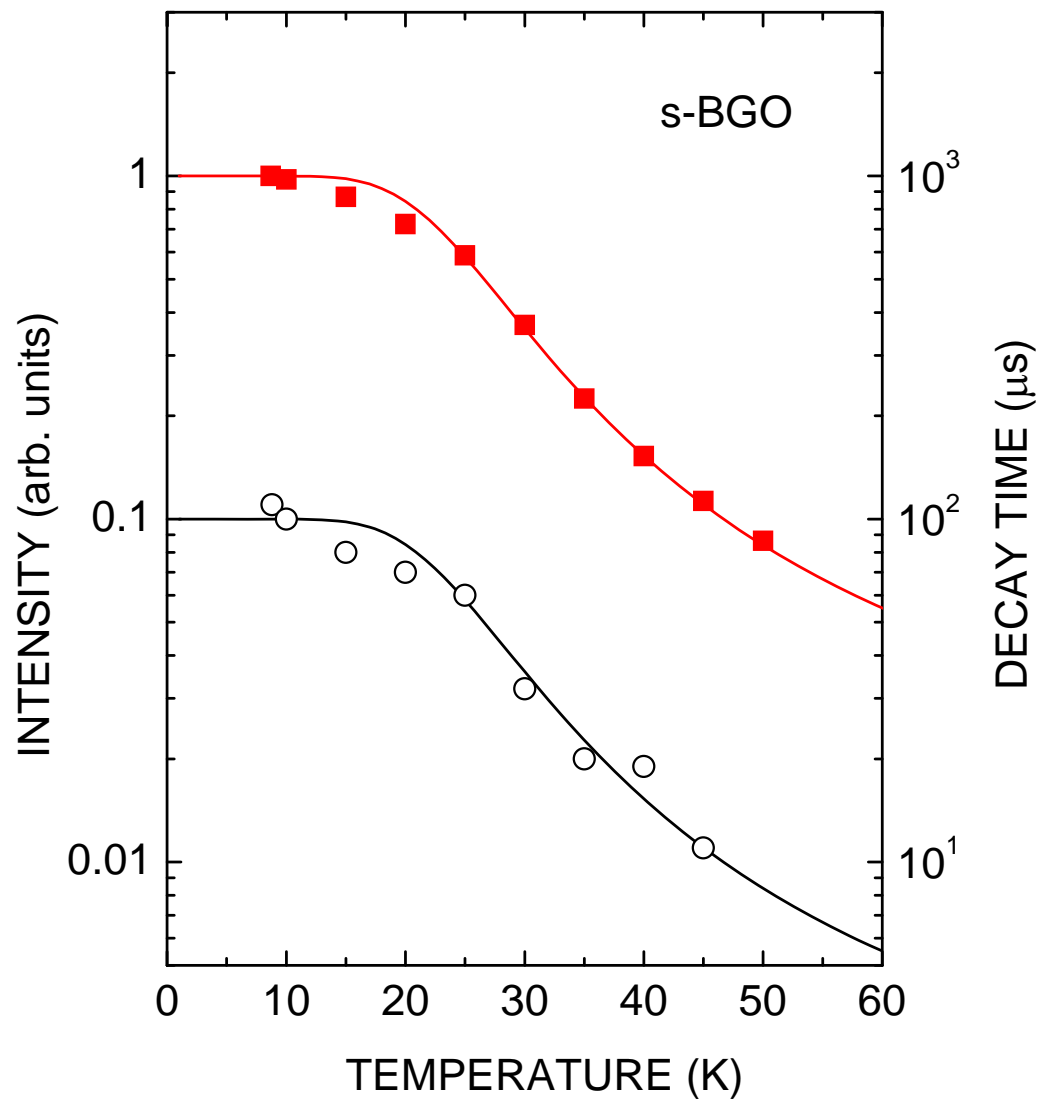


Figure 10

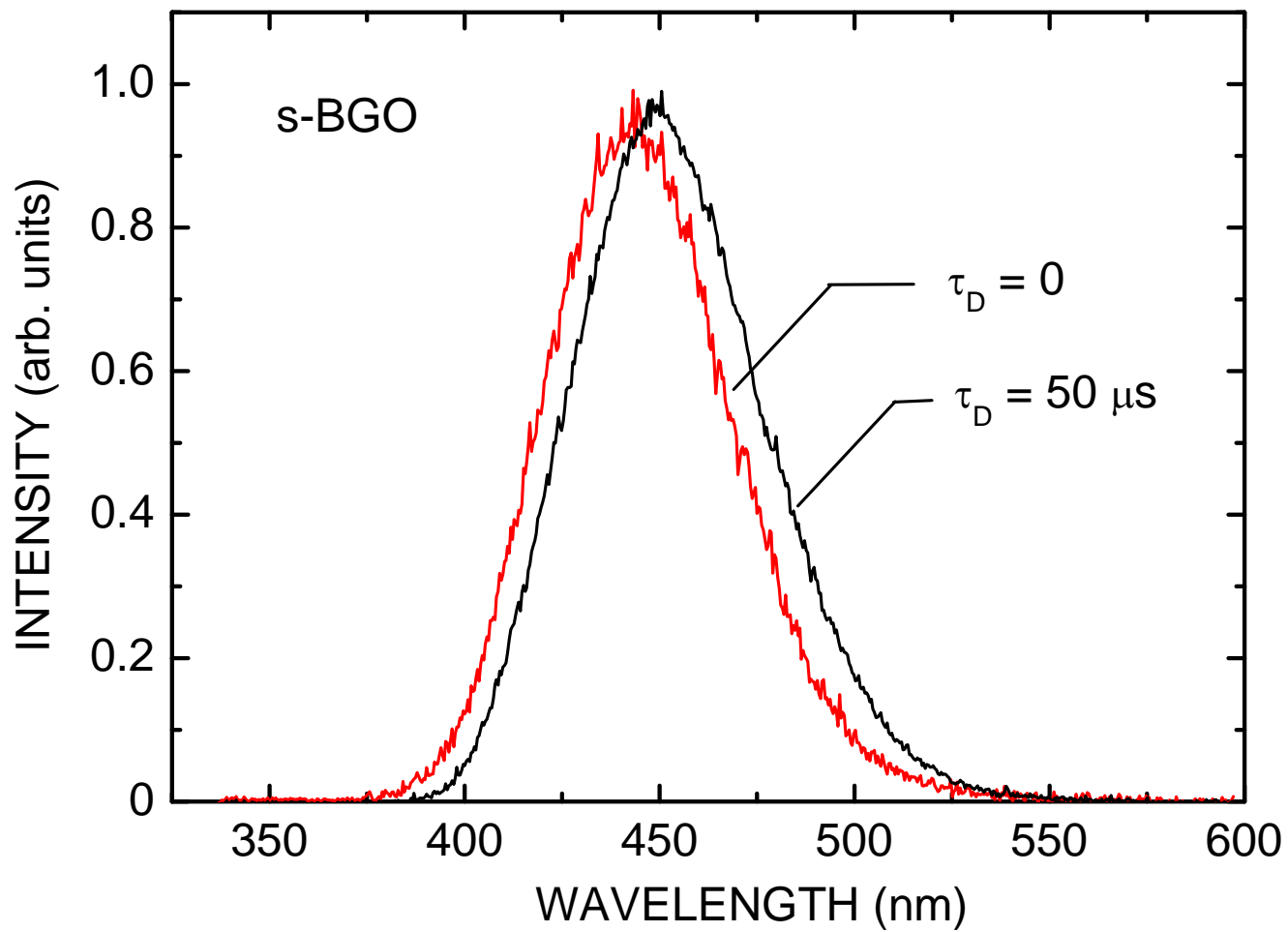


Figure 11

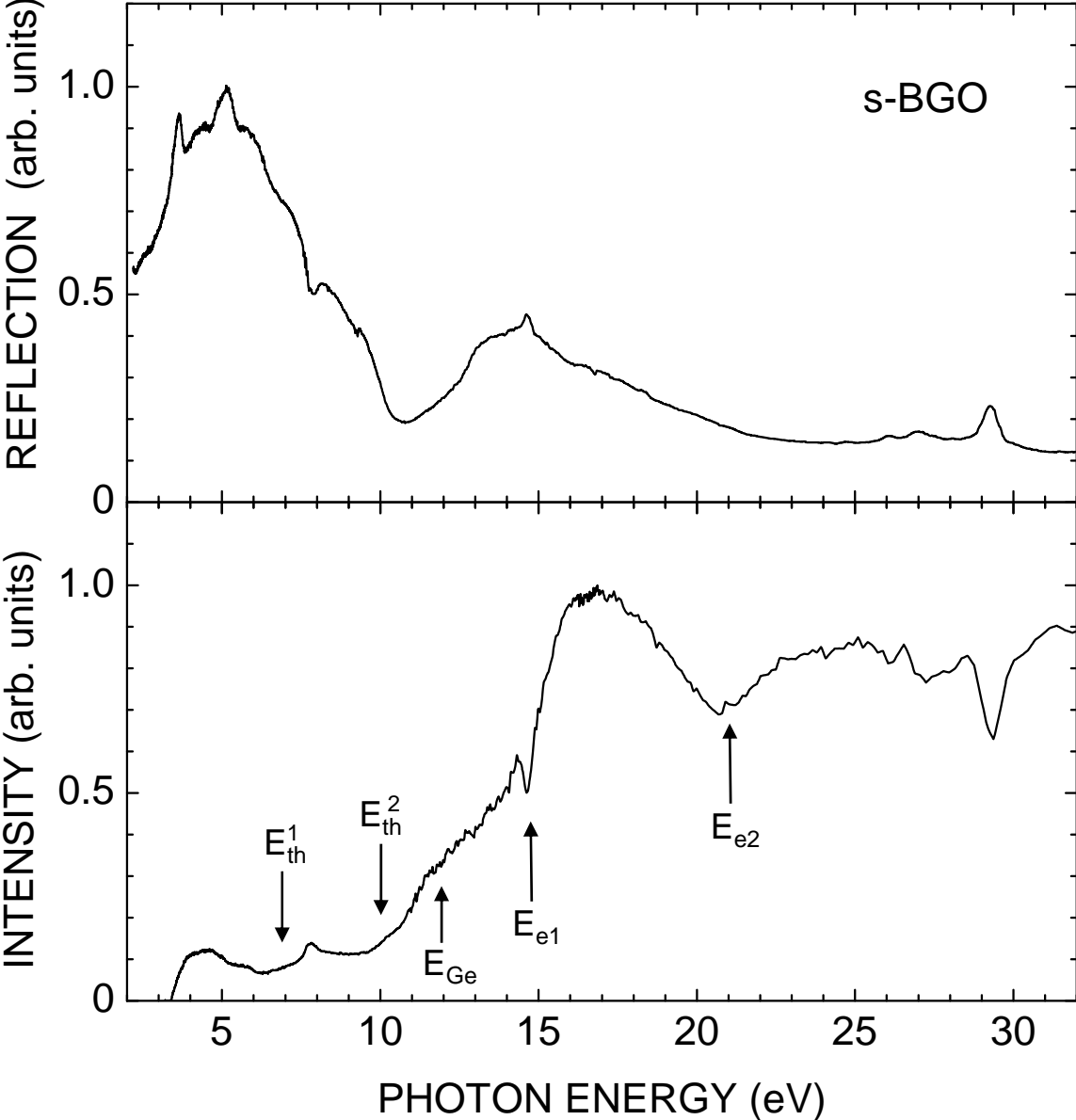


Figure 12

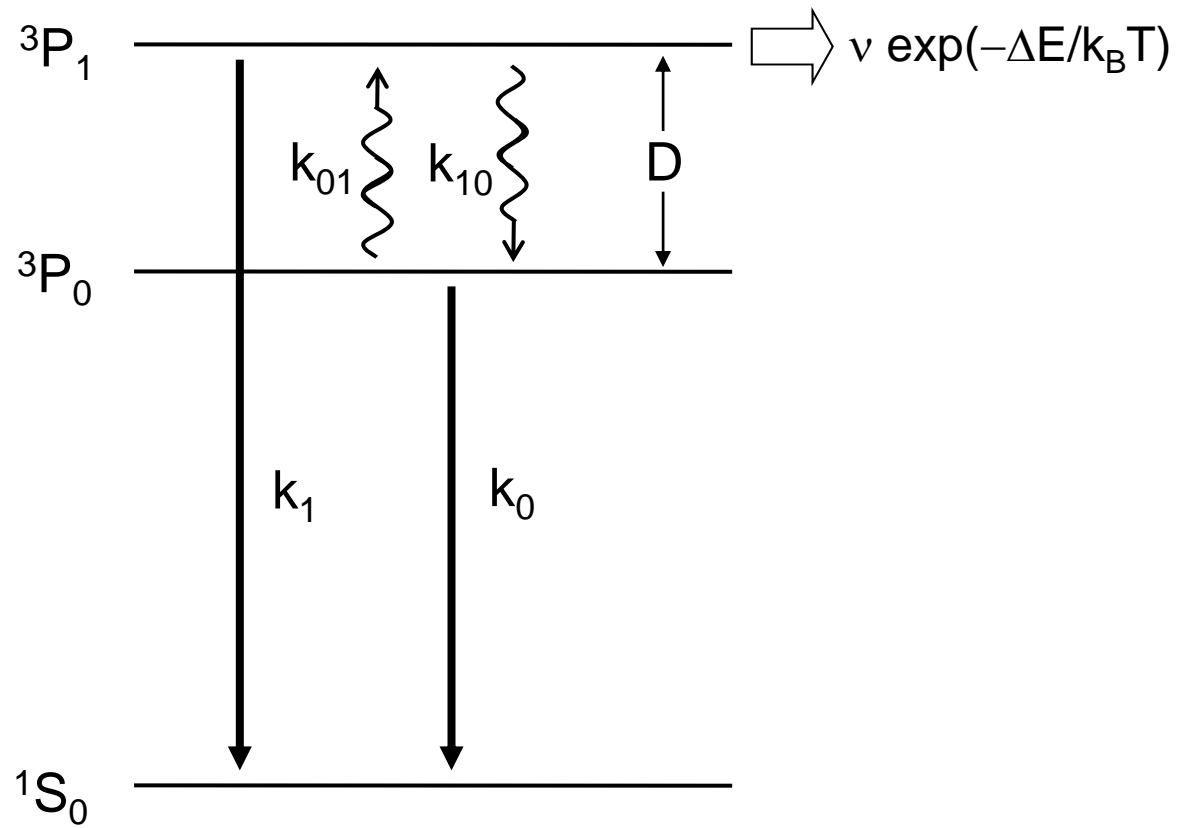


Figure 13

